Chapter 6

Supernova Remnant 1E 0102.2–7219 in the Small Magellanic Cloud

6.1 Introduction

A multi-frequency radio study of the young oxygen-rich supernova remnant 1E 0102.2–7219 has been undertaken using the ATCA. This is the highest resolution radio study undertaken to date. It has revealed new information concerning the morphology of this SNR, and has raised some questions about its classification.

The observations presented in Sections 6.2 and 6.3 along with a preliminary analysis of these data have been published by Shaun W. Amy[1] and Lewis Ball[2] in *The Astrophysical Journal*, volume 411, pages 761–766 in 1993.

6.1.1 Classification of Supernova Remnants

It is generally accepted that SNRs can be classified into four (or perhaps five) distinct categories based on direct observational evidence and parameters derived from observations. Mathewson et al. (1983a, 1983b & 1984), on the basis of a detailed study of SNRs in the Magellanic Clouds, suggested the following categories:

- Balmer-dominated,
- Oxygen-rich,
- Plerionic-composite, and
- Evolved.

Weiler & Sramek (1988) support these classifications but suggest, on the basis of a study of Galactic SNRs, that there is possibly a fifth class which they term centrally-influenced.

[1]School of Physics, University of Sydney, NSW 2006, Australia.
[2]Research Centre for Theoretical Astrophysics, University of Sydney, NSW 2006, Australia.

Balmer-dominated SNRs

These SNRs show filamentary optical structure with strong emission in the Balmer lines of hydrogen, but have little emission in either [O III] or [S II]. The morphology usually features a full or partial shell of filaments. They are also referred to as *Tychonic* SNRs after the well-known example SN1572 ("Tycho's remnant"). These are young SNRs and are thought to be due to Type Ia supernovae, generated by deflagrating white-dwarf stars.

They exhibit non-thermal radio emission (as do all SNRs) with a relatively steep spectral index of $\alpha \leq -0.3$ (where α is defined as $S \propto \nu^{+\alpha}$). Radio images show either a full or partial shell in the continuum. The radio emission from these SNRs is linearly polarized (as from most SNRs). The inferred magnetic field structures from young Balmer-dominated SNRs is generally radial.

At X-ray wavelengths, these SNRs show thermal emission. Both shell and centre-filled examples are observed. The X-ray emission is thought to be caused by the emission of high-velocity material causing a non-radiative shock in the neutral gas surrounding the exploded star.

Oxygen-rich SNRs

As the name suggests these supernova remnants are characterized by strong oxygen emission, specifically in [O III]. However, they show little or no emission in Hα or [S II] even though they are usually located near H II regions. These SNRs are thought to result from the explosion of a massive star giving rise to oxygen-rich ejecta from CNO processed material from deep within the stellar core. There are less than ten SNRs that are described as "oxygen-rich" of which Cassiopeia-A is the best known example. Like the Balmer-dominated SNRs, oxygen-rich SNRs are also shock driven. However, it is generally thought that the shock is interacting more with the circumstellar material ejected from the star in its final stages of evolution, rather than with matter swept up from the interstellar medium as in Balmer-dominated SNRs.

The radio characteristics of oxygen-rich SNRs are similar to those shown by Balmer-dominated SNRs. Oxygen-rich SNRs usually exhibit very high luminosity thermal X-ray emission and both filled and shell X-ray forms have been observed.

Plerionic-composite SNRs

These SNRs consist of a filled-centre (plerion) surrounded by a full or partial shell. These SNRs are quite different from the classes of SNRs discussed above in that the central component is believed to be powered by a neutron star (pulsar) while the surrounding shell is powered by shock processes. The central component is often extended.

The radio spectral index of the shell is relatively steep, $\alpha \leq -0.3$. The plerionic component generally has a flatter spectrum $\alpha \geq -0.3$. Because of this composite nature, the magnetic field structure is necessarily complex, with a radial or tangential magnetic field in the shell and a uniform magnetic field in the central component. At optical wavelengths, these SNRs show non-thermal continuum from the plerionic

component and thermal emission from the filaments in the surrounding shell. The pattern at X-ray wavelengths is similar, with non-thermal X-ray emission from the central component and thermal emission from the surrounding matter. The X-ray emission is generally concentrated towards the central component but may feature some extended emission in an outer shell.

Pure plerions can be considered as a sub-class of the above. The best example of a plerionic SNR is the Crab, the remnant of SN1054.

Evolved SNRs

This class of SNRs generally covers those which exhibit a partial shell shape. The emission arises from the interaction of modest velocity shock waves ($50 - 200\,\mathrm{km\,s^{-1}}$) with cloudlets in the ISM. It is likely that members of the above three classes of SNRs become "evolved SNRs" before fading below detectable limits. Both the Balmer-dominated and oxygen-rich SNRs already exhibit a shell morphology, and the plerionic-composite SNRs are expected to exhibit a pure shell-type morphology once the central component fades away.

In general, the characteristics of evolved SNRs are similar to those of the other three categories already discussed. The main difference at radio wavelengths is that the inferred magnetic field direction in evolved SNRs is mixed, as expected for older SNRs. At optical wavelengths the main distinguishing observational feature is that the [S II]/Hα ratio is usually > 0.7 which is relatively high. In X-rays, thermal emission with a partial shell form is often seen.

Centrally-Influenced SNRs

This fifth class of SNRs has been suggested by Weiler & Sramek (1988). The morphology of these remnants is generally shell-shaped but is heavily influenced by the presence of a central, strong, compact X-ray emitting source. Models have been proposed in which precessing jets or beams from a central compact object (such as a pulsar) can significantly affected the SNR morphology. The best known example of this type of object is W50 (G39.7–2.0).

6.2 Previous Studies of SNR 1E 0102.2–7219

The object 1E 0102.2–7219 was identified as a possible SNR in an X-ray survey of the SMC by Seward & Mitchell (1981). This was part of a larger survey of around 40 square degrees using the imaging instruments on board the *Einstein Observatory*. The detector used for the major portion of the survey was the Imaging Proportional Counter (IPC) which has a spatial resolution of about 1 arcmin and is sensitive to X-ray energies in the range from $0.15 - 4\,\mathrm{keV}$. The identification was made on the basis of its luminosity (2.1×10^{37} ergs s^{-1} in the $0.2 - 2\,\mathrm{keV}$ band) and the spectral energy distribution. SNR 1E 0102.2–7219 is the second brightest X-ray source in the SMC.

Following the X-ray detection, Dopita et al. (1981) used the Anglo-Australian Telescope with narrow band filters to image 1E 0102.2–7219 in the Hα, [O III] λ5007 and [S II] $\lambda\lambda$6717, 6731 emission lines. These images revealed a large [O III]/Hα ratio with a strong [O III] filamentary shell some 1.5 arcmin from the X-ray position determined from the *Einstein* survey. There was no detectable emission in [S II]. On the basis of these observations, Dopita et al. (1981) classified the remnant as a member of the oxygen-rich class of SNRs. Of the small number of members of this class, two lie in the LMC (0540–693 and N132D). SNR 1E 0102.2–7219 is unique in that it is the only oxygen-rich SNR in the SMC.

Previous studies at radio wavelengths have searched for the expected non-thermal emission associated with this SNR. However, the observations have been hampered by confusion with the nearby bright H II region N76 (Henize 1956) located just to the south-west of the SNR. The relatively strong thermal emission from this extended H II region has dominated previous single-dish measurements at 6.0 cm and 3.4 cm undertaken at Parkes (McGee, Newton & Butler 1976). For this reason, we have undertaken high resolution radio observations with the MOST and ATCA.

6.3 Radio Observations

6.3.1 The MOST 843 MHz Image

The radio observations at 843 MHz were made as part of a program to survey the Small and Large Magellanic Clouds. The details of the instrument have been discussed in Chapter 2. The raw data were reduced using locally developed software (the $\mathcal{MSYN}$ package) which produces a raw (or dirty) image and corresponding beam (or point-spread function). These can then be loaded into a standard astronomical software reduction package such as $\mathcal{AIPS}$ (Astronomical Image Processing System) for further processing which includes deconvolution, display and plotting. A number of techniques routinely applied to synthesis data from radio interferometers are not applicable to MOST data, although in some cases alternative algorithms such as self-calibration have been developed.

Figure 6.1 shows the contour image of 843 MHz radio emission from SNR 1E 0102.2–7219 after deconvolution with the CLEAN algorithm (as implemented by the $\mathcal{AIPS}$ task `APCLN`). At the resolution of the MOST (approximately 44″) the SNR appears to be only slightly extended and is projected onto and perhaps embedded in the H II region N76.

6.3.2 A Preliminary ATCA Image at 4790 MHz

A preliminary higher-resolution study of SNR 1E 0102.2–7219 was undertaken soon after the ATCA was commissioned, as part of a program to observe a small number of SNR candidates in the Magellanic Clouds. Although this was a known SNR at the time, it was included as part of these observations to determine the nature of the source

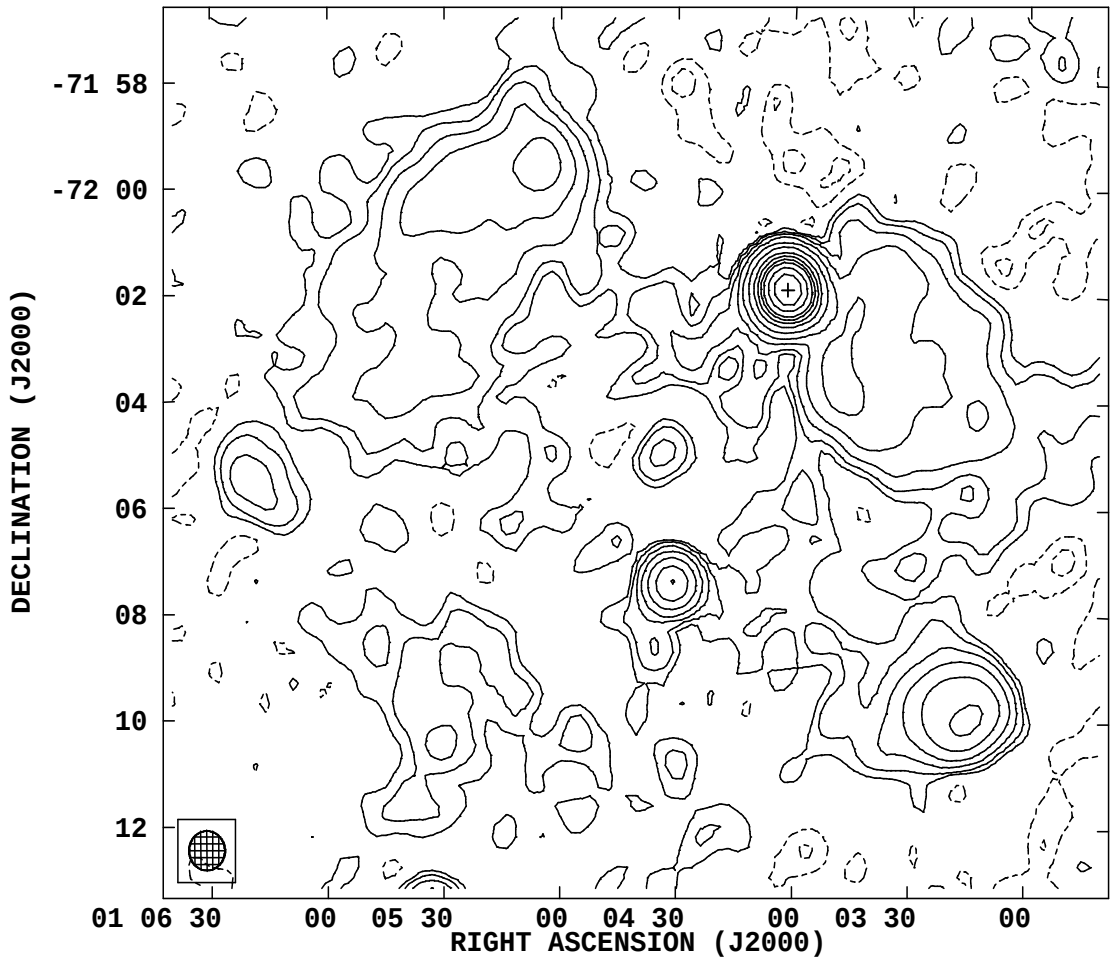

Figure 6.1: The MOST 843 MHz image of SNR 1E 0102.2–7219. The HPBW is 44.5 × 42.5 arcsec and is shown in the lower-left corner. The contour levels are −4, −2, −1, 1, 2, 4, 8, 16, 30, 50, 70, 90, 110, 150, and 200 mJy/beam. The SNR, which is denoted by the cross, appears to be embedded in the large H II region N76.

at the higher angular resolution of the ATCA.

At the time these observations were made, only 5 of the 6 antennas which comprise the ATCA had been commissioned, so the maximum baseline was 3 km and the total number of baselines was 10. Observations in either the 6 cm (4.8 GHz) or 3 cm (8.6 GHz) band were possible although dual frequency operation was not possible. The lower frequency was chosen to gain a higher flux from the non-thermal synchrotron radiation. It was also considered possible that thermal emission at 3 cm would have dominated any non-thermal radiation. Thus an observing frequency of 4790 MHz was chosen with the standard ATCA continuum bandwidth of 128 MHz. The phase centre was deliberately offset from the SNR position to avoid problems with instrumental effects occurring at the phase centre (such as DC offsets caused by the correlator). Since the SNR was still located near the phase centre and because the bandwidth was a small fraction of the observing frequency, bandwidth smearing was not expected to be significant. All the frequency channels were therefore averaged to a single channel (often referred to as the "channel zero" dataset) early in the data reduction phase.

A summary of the observations is given in Table 6.1. Flux calibration was achieved by reference to the standard ATCA primary flux calibrator PKS B1934–638. A recent re-analysis of the flux density of PKS B1934–638 has been undertaken by Reynolds (1994) which gives the flux density of PKS B1934–638 as 6.3 Jy at 4790 MHz. The primary phase calibrator chosen was PKS B0047–579, which was also used as a secondary flux calibrator. A typical observing session would involve a short observation (e.g. five minutes) of the secondary calibrator followed by a lengthy integration on the target source. The total calibrator-target cycle would either be around 30 or 60 minutes and then repeated throughout the observing session. At some stage during the observing session, a short integration (around 15 minutes) on the primary flux calibrator would also be undertaken.

The data were reduced entirely in $\mathcal{AIPS}$ using techniques developed for the ATCA as detailed in Killeen (1993). Data from different configurations were obtained, and were reduced in a similar manner to enable the merging of the separately calibrated datasets before imaging, deconvolution and analysis. In contrast to ATCA data obtained more recently, considerable editing was required to remove bad visibilities caused largely by instrumental problems.

Table 6.1: Overview of the preliminary ATCA 4790 MHz observations of SNR 1E 0102.2–7219

Observation Date	ATCA Configuration	Approximate observing time
1990 May 03	1	11×8 min
1990 Aug 22	2	12×52 min
1990 Sep 21	3	14×30 min
1991 Jan 23	4	3×52 min
1991 Apr 25	3A	3×52 min

The resulting grey-scale total intensity (i.e. Stokes I) image (after deconvolution using the CLEAN algorithm) is presented in Figure 6.2. This 4790 MHz image is shown with overlaid contours. For display purposes the image shown has been interpolated onto a finer grid. As expected the nearby H II region, N76, has been resolved out.

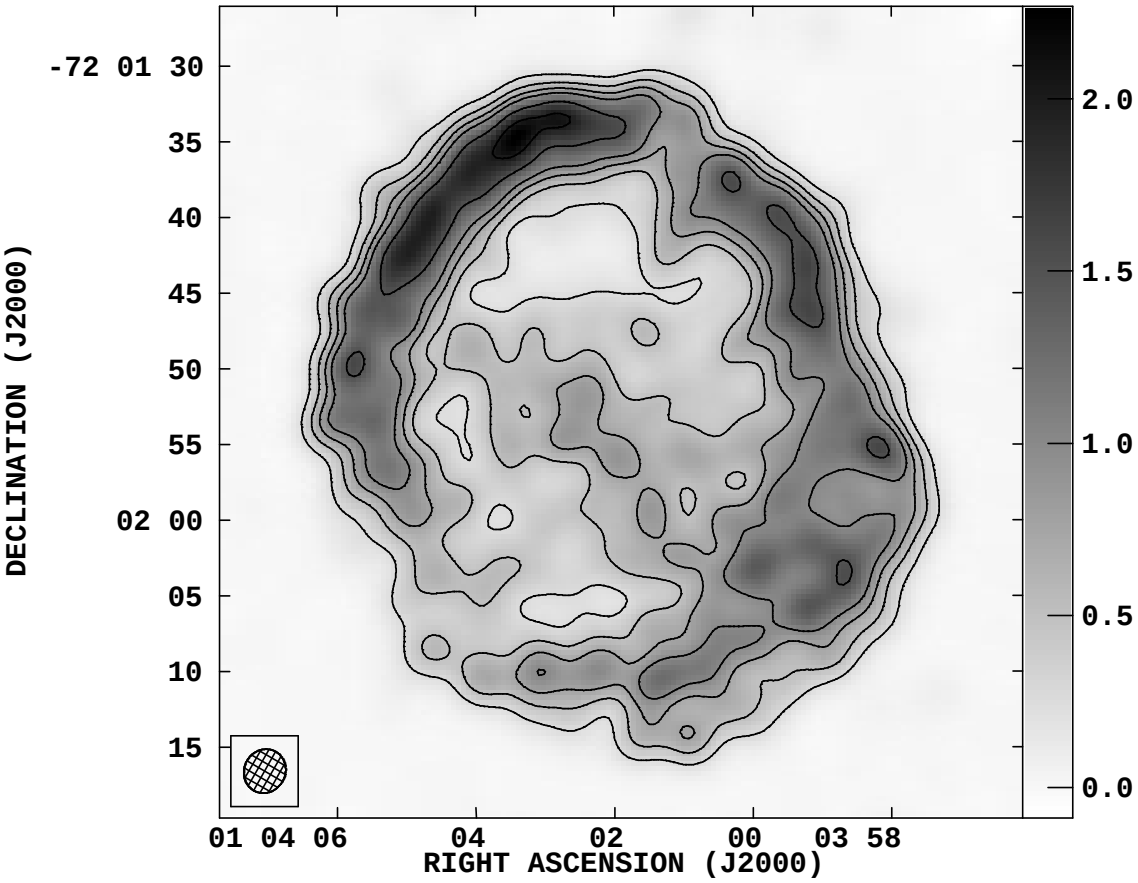

Figure 6.2: The preliminary ATCA 4790 MHz total intensity image of SNR 1E 0102.2–7219. The HPBW is approximately 2.75 × 2.96 arcsec (p.a. −29.8 degrees). The H II region, N76, is smooth enough to be essentially resolved out and so is not seen here. The contour levels are −10, −8, −6, −4, −3, −2, −1.5, −1, −0.75, −0.5, −0.25, 0.25, 0.5, 0.75, 1, 1.5, 2, 2.5, 3 mJy/beam and the grey-scale (linear) transfer function is indicated by the wedge on the right. The rms noise is around 7.5×10^{-2} mJy/beam.

An alternative presentation of the image is given in Figure 6.3 in which a three-dimensional surface plot is shown looking towards the SNR from an elevated position to the south-east. The most striking feature of both Figures 6.2 and 6.3 is the almost complete shell of emission. Somewhat less obvious, but nonetheless clearly shown in both figures, is what appears to be a relatively compact central component.

To better illustrate the presence of this compact central component and its relative intensity compared to the shell, one-dimensional slices in right ascension and declina-

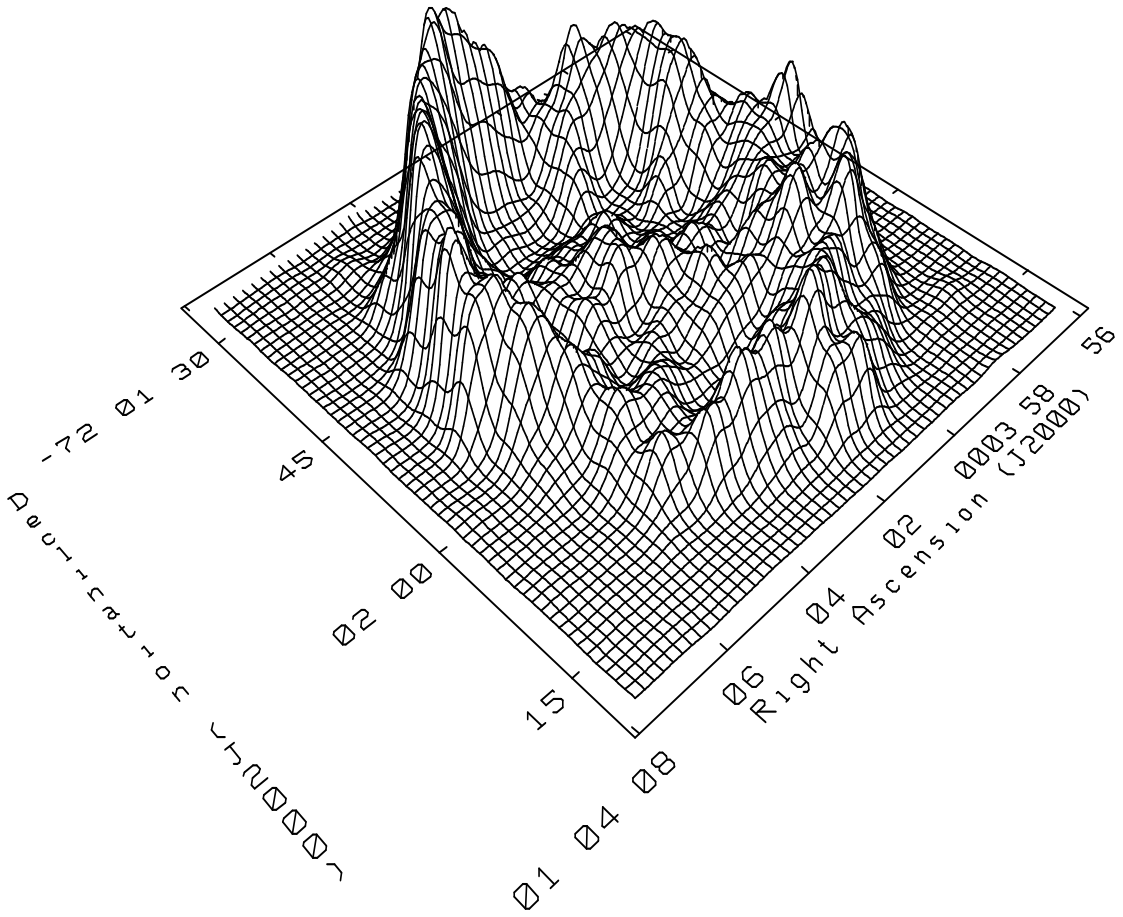

Figure 6.3: The preliminary ATCA 4790 MHz total intensity image of SNR 1E 0102.2–7219 (as shown in Figure 6.2) displayed as a three-dimensional surface plot. Note the presence of a relatively strong compact component in addition to an almost complete shell.

tion, are shown in Figure 6.4. The two slices, taken at arbitrary positions, illustrate the intensity and extent of the central component.

6.4 A High-Resolution Multi-Frequency Study with the ATCA

The observations of SNR 1E 0102.2–7219 detailed above demonstrated the imaging power of the ATCA and revealed new morphological information regarding this source. To better understand the nature of this SNR, multi-frequency data were needed. A decision was made to attempt to map the distribution of magnetic field by undertaking polarization observations. A proposal for these observations was submitted to the ATCA. An independent proposal by Dr M.A. Dopita (Mount Stromlo and Siding Springs Observatory) and Dr D.K. Milne (Australia Telescope National Facility) to observe SNR 1E 0102.2–7219 at two frequencies, and to map the magnetic field distribution was submitted at the same time. At the suggestion of the AT time assignment committee, a collaboration between the two groups was established. The work described in this section comprises the results obtained through this collaboration, although the analysis has been done solely by the author.

6.4.1 Observing Strategy and Data Reduction

At the time of the observations (1992), dual frequency operation of the ATCA was possible, although some of the on-line phase correction hardware was not available for the second frequency. This did not have any significant detrimental effect on the data. It was also possible to remotely rotate the turrets housing the feed and receiver packages, thus allowing the possibility of observing in all four ATCA bands during a single observing session. A total of five observing sessions was allocated with four different telescope configurations. Two separate observations each of 12 hours were allocated for one of the configurations. Frequency switching between bands was thus not necessary for that configuration and the standard ATCA dual frequency mode was used. Further details of the observations are given in Table 6.2.

Table 6.2: Overview of the ATCA multi-frequency observations of SNR 1E 0102.2–7219

Observation Date	ATCA Configuration	Bands (cm)	Reference Antenna
1992 Mar 20	6A	6,3,13,20	CA05
1992 Mar 31	6C	6,3,13,20	CA05
1992 Jun 05	1.5D	6,3	CA03
1992 Jun 07	1.5D	13,20	CA04
1992 Jun 19	1.5B	6,3,13,20	CA04

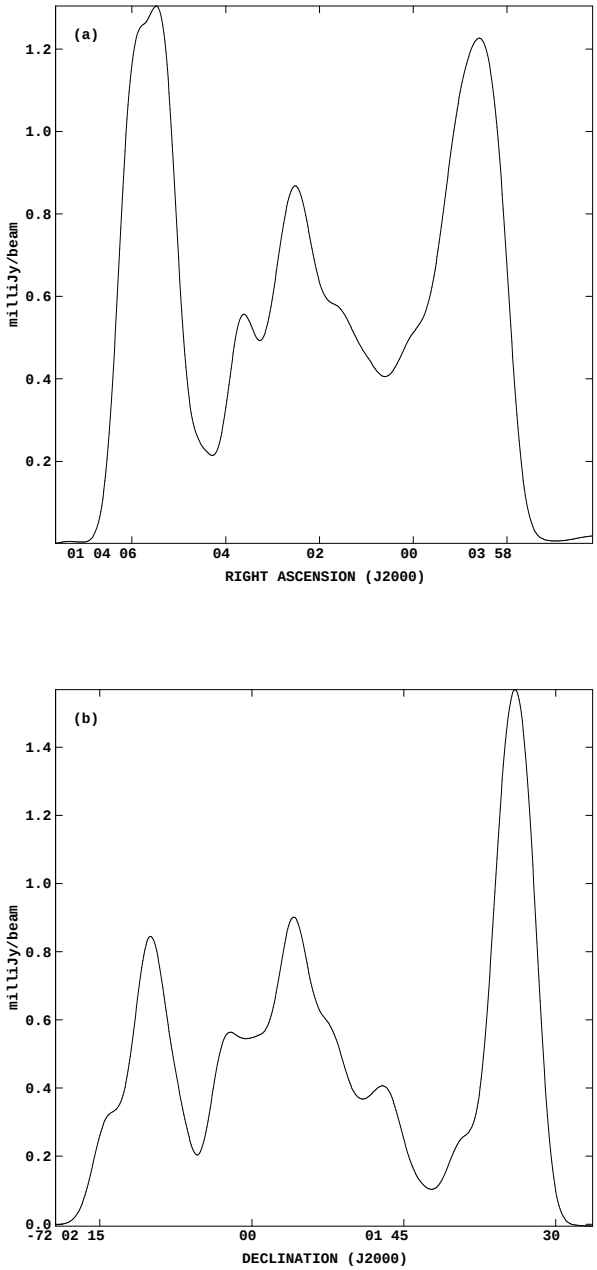

Figure 6.4: Cross-cuts through the preliminary ATCA 4790 MHz total intensity image (as shown in Figures 6.2 and 6.3) with (a) showing a cut in right ascension and (b) showing a cut in declination. Note again the relatively strong compact central component.

As with the earlier (single-frequency) observations, the flux calibration was achieved with reference to PKS B1934–638. A short (10 minute or so) observation of this source was made during each run, at each of the observed frequencies. The basic observing cycle consisted of 25 minutes on the target source followed by 4-5 minutes observing a secondary calibrator, used primarily for phase calibration. This source was PKS B0252–712 which is nearby and has an accurate VLBI-based position. In addition, a brief observation of a polarization calibrator was undertaken at all four frequencies. The source 3C286 (B1328+307) was chosen. Although this is a northerly source, and it takes significant time to drive to and from the polarization calibrator, it was one of only two recommended polarization calibration sources for the ATCA (both of which are situated to the north). This source is only visible for a few hours each day. Experience with ATCA data has now revealed that there are no significant gains in observing a polarization calibrator and it is no longer part of the recommended observing procedure. Nonetheless these data were reduced using the polarization gain and leakage terms determined from the short observation of 3C286.

Each observation was reduced independently with the following steps being undertaken for each dataset.

1. The ATCA-specific *AIPS* task `ATLOD` was used to determine a best estimate of the relative phase difference between each feed of each antenna (commonly referred to as the XY-phase) and the system temperature. Although both values are measured "on-line", the hardware available at the time of these observations (i.e. prior to November 1992) led to a somewhat noisy and thus inaccurate measurement, with frequent dropouts and/or bad data. Although the XY-phase parameter is not essential it does assist with the gain and polarization calibration. The resulting values were plotted (using the standalone program `pltsys`) to determine a best estimate of the value for each antenna at each frequency. A median value, which is less susceptible to outliers than the average, was typically used. This was derived from the above plots.

2. The data were then loaded into *AIPS* using `ATLOD`, with the XY-phase values determined as above used to override the on-line values. In addition, the on-line measured system temperatures were averaged using a running-mean to improve the accuracy of these data, which are typically noisy on the timescale of a single integration (i.e. 15 s). As *AIPS* can only correctly handle circular polarizations, the input linear polarizations were re-labelled as circular polarizations. The polarization calibration (and final data editing) were later done using *MIRIAD* which can handle linear polarizations correctly.

3. The resulting *AIPS* dataset was listed using `LISTR` to check the consistency of the scans with that which were observed, and `SETJY` was used to set the flux scale of PKS B1934–638 at all frequencies.

4. A quick inspection of the data as a function of frequency across the band was obtained by using `POSSM` for both the primary and secondary calibrator. These

plots were used to check for interference and to choose a suitable range of channels for later averaging of the multi-channel dataset. The most apparent problem was quite severe interference in the 20 cm band over a small range of 3–5 channels (out of a total of 32 channels). This interference mostly affected 2–3 of the shorter baselines out of a total of 15.

5. Rather than removing the whole of the affected baseline, `SPFLG` was used to excise only the channels containing the interference. This demonstrates an obvious advantage of using a telescope such as the ATCA which always operates as a spectral line instrument, even for "continuum" observations. This feature is particularly valuable when there are only a small number of total baselines, especially since the shorter baselines are needed to image the large scale structure often present in SNRs.

6. These data were then averaged into a so-called "Channel-0" dataset (using `AVSPC`). In this step the frequency channels are averaged to a single central frequency channel.

7. The data were then flagged using `TVFLG` using the amplitude difference flagging option based on the deviations from a running mean of a few integrations. This makes the flagging process less susceptible to large changes in amplitude levels which are experienced between calibrator and a (weak) target source. If there were bad data for a single polarization (say RR) then `TVFLG` was configured to flag not only RR but also the other three polarizations LL, RL and LR. Note that although these are labelled with $\mathcal{AIPS}$ as components of circular polarization, the ATCA has linearly polarized feeds. This is crucial to ensure correct results when combining the measured components to form the Stokes parameters. In general the 6 cm and 3 cm data were of high quality with little flagging needed. The 13 cm data were of reasonably high quality with short periods of interference. Unfortunately, the 20 cm data were generally of rather poor quality, with much of the data being badly affected by various sources of interference.

8. The resulting (flagged) multi-source, multi-frequency files were then separated using `SPLIT` into single-source, single-frequency datasets and written to disk (using `FITTP`) as FITS format files for loading into $\mathcal{MIRIAD}$ where further calibration, imaging, deconvolution and analysis took place.

9. The $\mathcal{MIRIAD}$ task `gpcal` was used to determine the XY-phase residuals and the instrumental polarization from the observations of the secondary calibrator. The options used were `refant = 5, minants = 4, interval = 5` and `options = xyvary, qusolve`. These task parameters define the reference antenna, the number of antennas necessary before a solution is attempted, the solution interval and the XY-phase is permitted to vary with time and to solve for Q and U fluxes as we have good parallactic angle coverage.

10. To determine the success of this calibration the results were inspected using `gpplt` by looking at the ratio of the phase of the X-feed gain to the Y-feed gain. To achieve this the `yaxis` parameter was set to `phase` and the `options` parameter set to `xygains`.

11. Preliminary images were made of the secondary calibrator (using `invert`) to inspect the quality of the data and this also gave a value for the theoretical RMS noise. This was then compared to the value as determined from the task `histo`.

12. These images and a comparison of the theoretical noise to actual noise on the image were then used to determine the success of the flagging conducted earlier. If required, the task `uvplt` was used to determine if bad data remained and `uvflag` used to excise these data. The images were then re-made and the noise comparison and qualitative inspection conducted again until the images were deemed to be of high enough quality.

13. The above solutions for antenna gains and polarization leakages were copied to 3C286 (the polarization calibrator) using `gpcopy` with the `options` parameter `unset`.

14. The *MIRIAD* task `gpcal` was then run on the polarization calibrator with the `options` parameter set to `nopol, xyref, polref, noxy` which means, respectively, do not solve for the instrumental polarization leakage characteristics, solve for the XY-phase of the reference antenna, solve for the instrumental polarization leakage of the X-feed of the reference antenna and do not solve for any XY-phase offset. This combination of parameters means that `gpcal` solves for the X-feed of the reference antenna only.

15. Copy these solutions to the primary calibrator (in this case PKS B1934–638) using `gpcopy`.

16. Run `gpcal` with the options `nopol, noxy` to determine the flux density of the primary calibrator.

17. Use `gpboot` to bootstrap the flux of the secondary calibrator (which applies a simple scaling factor).

18. Interpolate these solutions onto the programme source using `gpcopy` which should now have been correctly calibrated for both amplitude and phase and allow Stokes parameters to be correctly calculated.

19. Further inspection (using `uvplt` and editing (if required) of the programme source UV data was undertaken using `uvflag`. To ensure that the corresponding visibilities of the other Stokes' components were also flagged using `uvpflag`.

20. Image analysis and presentation were then carried out entirely within *MIRIAD*.

6.4.2 Total Intensity Images

The resulting total intensity images at the four observed frequencies are shown at the observed resolution in Figures 6.5, 6.6, 6.7 and 6.8.

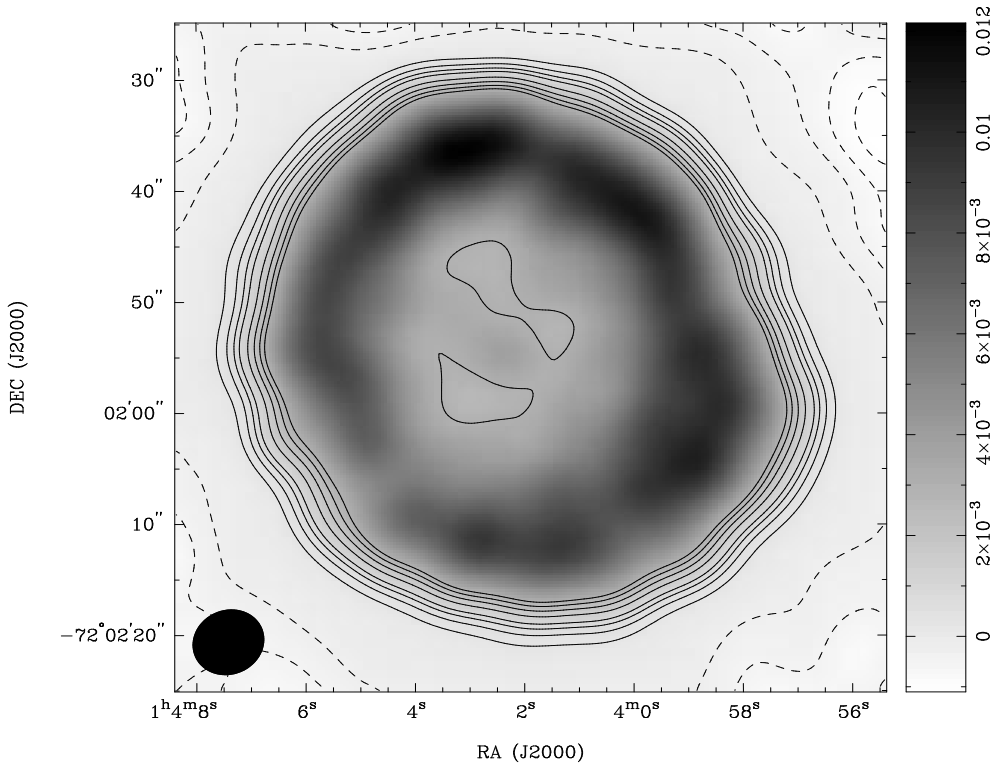

Figure 6.5: The multi-configuration ATCA image of SNR 1E 0102.2–7219 at 1472 MHz. The HPBW is approximately 6.26 × 5.73 arcsec (p.a. −53.1 degrees) and is shown in the bottom-left corner. The (linear) transfer function is indicated by the wedge on the right with intensity units of Jy/beam. Contours have been overlaid at −10, −8, −6, −4, −3, −2, −1.5, −1, −0.75, −0.5, −0.25, 0.25, 0.5, 0.75, 1, 1.5, 2, 2.5, 3 mJy/beam.

Each image has been deconvolved using the *MIRIAD* task `clean`, restored using a Gaussian beam of the nominal resolution (using the *MIRIAD* task `restor`) and then displayed using `cgdisp` after a subimage was made of the region of interest with `imsub`. All four images show the general shell-like structure of an SNR with the expected decrease in total flux as frequency increases. Features of interest common to all images are an area of enhanced emission in the north-east quadrant, and a "gap" in the almost otherwise complete shell of emission to the south-east. There is some evidence that there is a greater contribution to the total flux from the region *inside* the shell as the frequency increases, which possibly supports the earlier argument that there maybe a compact central component.

The apparently poor quality of the 3 cm image is most likely due to the fact that the source is quite weak; the surface brightness of SNR 1E 0102.2–7219 is not significantly

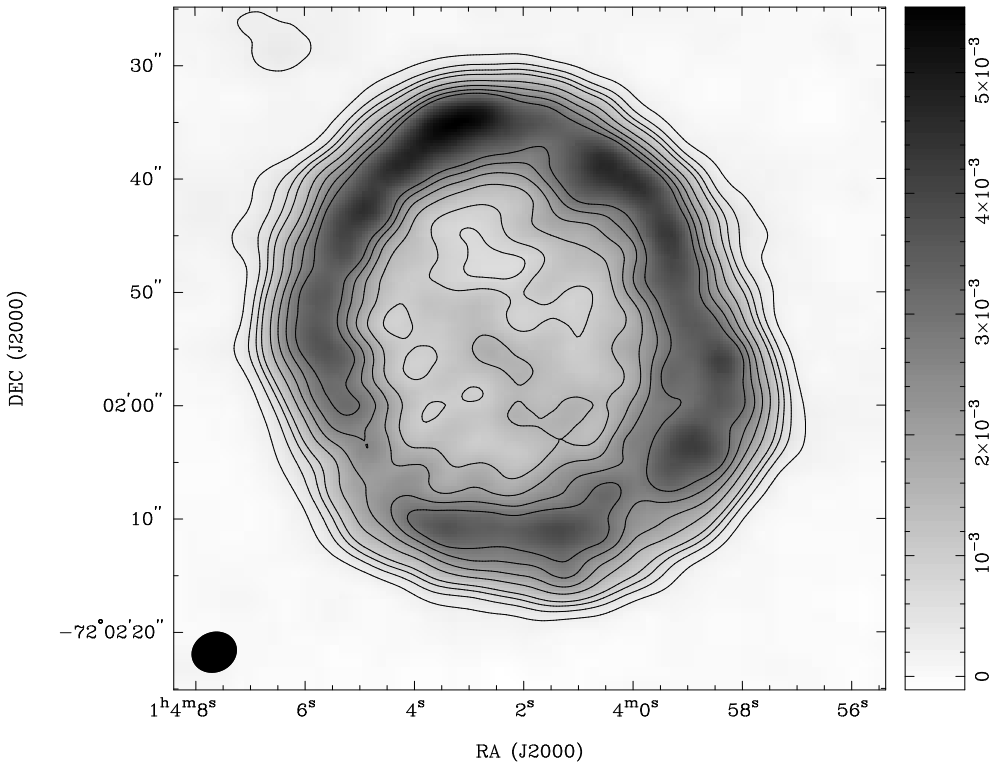

Figure 6.6: The multi-configuration ATCA image of SNR 1E 0102.2–7219 at 2368 MHz. The HPBW is approximately 3.95 × 3.52 arcsec (p.a. −59.1 degrees) and is shown in the bottom-left corner. The (linear) transfer function is indicated by the wedge on the right with intensity units of Jy/beam. Contours have been overlaid at −10, −8, −6, −4, −3, −2, −1.5, −1, −0.75, −0.5, −0.25, 0.25, 0.5, 0.75, 1, 1.5, 2, 2.5, 3 mJy/beam.

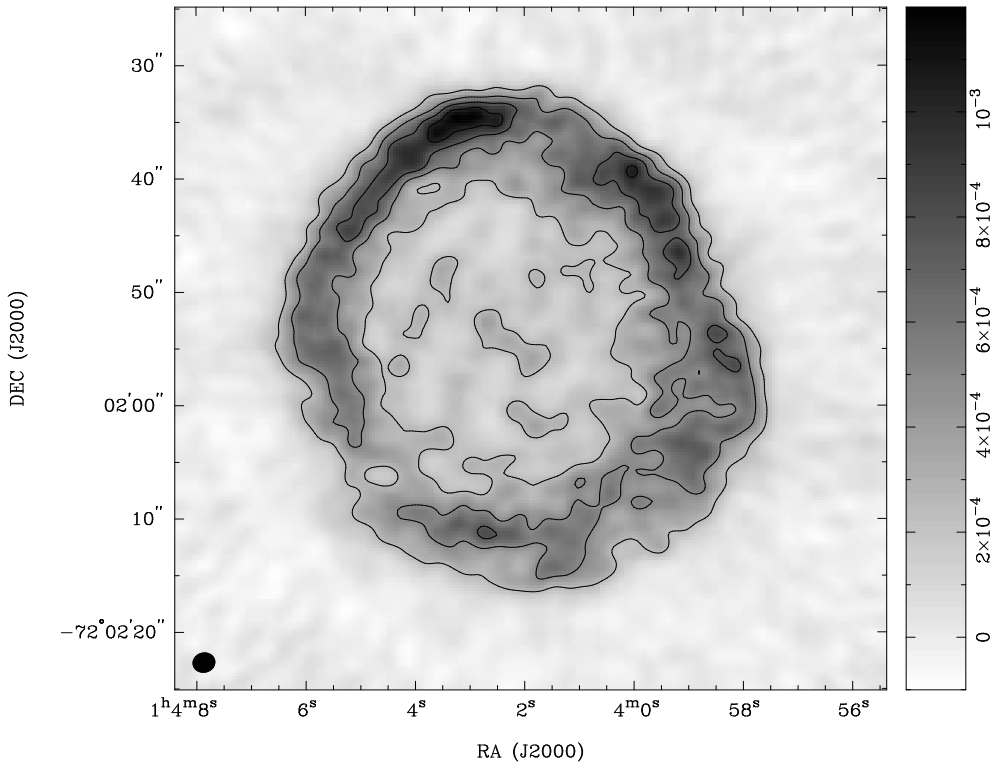

Figure 6.7: The multi-configuration ATCA image of SNR 1E 0102.2–7219 at 4790 MHz. The HPBW is approximately 1.95 × 1.78 arcsec (p.a. −71.2 degrees) and is shown in the bottom-left corner. The (linear) transfer function is indicated by the wedge on the right with intensity units of Jy/beam. Contours have been overlaid at −10, −8, −6, −4, −3, −2, −1.5, −1, −0.75, −0.5, −0.25, 0.25, 0.5, 0.75, 1, 1.5, 2, 2.5, 3 mJy/beam.

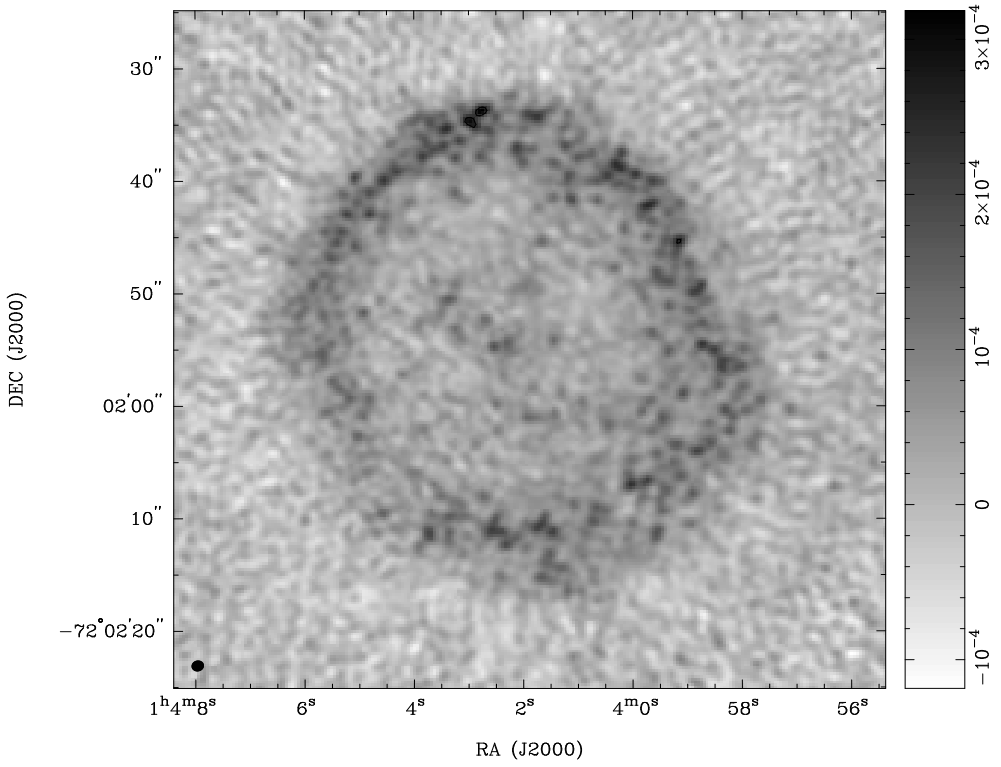

Figure 6.8: The multi-configuration ATCA image of SNR 1E 0102.2–7219 at 8640 MHz. The HPBW is approximately 1.06 × 0.97 arcsec (p.a. −71.0 degrees) and is shown in the bottom-left corner. The (linear) transfer function is indicated by the wedge on the right with intensity units of Jy/beam. Contours have been overlaid at −10, −8, −6, −4, −3, −2, −1.5, −1, −0.75, −0.5, −0.25, 0.25, 0.5, 0.75, 1, 1.5, 2, 2.5, 3 mJy/beam.

greater than the noise level in the image. The "spotty" effect is probably due to the cell size used when gridding the data during image formation. In this case 0.25 arcsec pixels were used in order to get 3-4 resolution elements spaced across the nominal resolution of the synthesized beam.

To better compare the images at the four frequencies, the higher frequency images were smoothed to the same resolution as that of the 1472 MHz image using the *MIRIAD* task `smooth`. These smoothed images are shown in Figure 6.9 together with the 1472 MHz image at the observed resolution.

6.4.3 Polarimetry

The intensity and structure of the magnetic field in supernova remnants varies markedly from object to object, and is the subject of considerable current interest. One of the aims of the multi-frequency study of SNR 1E 0102.2–7219 was to measure and characterize the magnetic field.

Despite exercising considerable care during the observing and data reduction, no significant polarization was detected. The results are limited solely by the signal-to-noise. For reference, the grey-scale total intensity images with *electric*-field vectors overlaid at all four frequencies are shown in Figure 6.10.

In some of the images there is a vague suggestion that some of the electric field vectors may be aligned but these are probably more of a chance occurrence rather than indicating polarized intensity. Given that the peak intensity of the 4790 MHz image is less than 1.5 mJy/beam, and that SNRs typically have a polarized intensity of no more than about 10%, it is clear that any polarized intensity will lie at a similar level to the rms noise in the image.

6.5 The Radio Spectrum

The integrated flux density from the preliminary ATCA image at 4790 MHz has been obtained from the deconvolved ATCA data using the AIPS verb `TVSTAT` which allows the region of interest to be enclosed inside a user-selected polygon. This procedure gave an estimated flux density at 4790 MHz of $S = 112$ mJy. The uncertainty in this estimate is difficult to determine but is probably between 5 and 10%. A similar procedure was used for the more recent multi-frequency ATCA data with the integrated flux densities obtained at all four frequencies. These are tabulated in Table 6.3.

Figure 6.11 shows a plot of the integrated flux densities of SNR 1E 0102.2–7219 obtained using the multi-frequency ATCA results together with previously published flux densities from the Mills' Cross at 408 MHz (Clarke, Little & Mills 1976) and from the MOST at 843 MHz (Ye 1988). In addition, the figure shows the best-fit power-law spectrum, $S \propto \nu^{+\alpha}$, to these data. If only the Mills' Cross, MOST and the preliminary ATCA data at 4790 MHz are used a spectral index of $\alpha = -(0.7 \pm 0.1)$ was determined whereas in the case where the more recent multi-frequency ATCA data is used along with the same lower frequency data the best-fit to the power-law spectrum was found

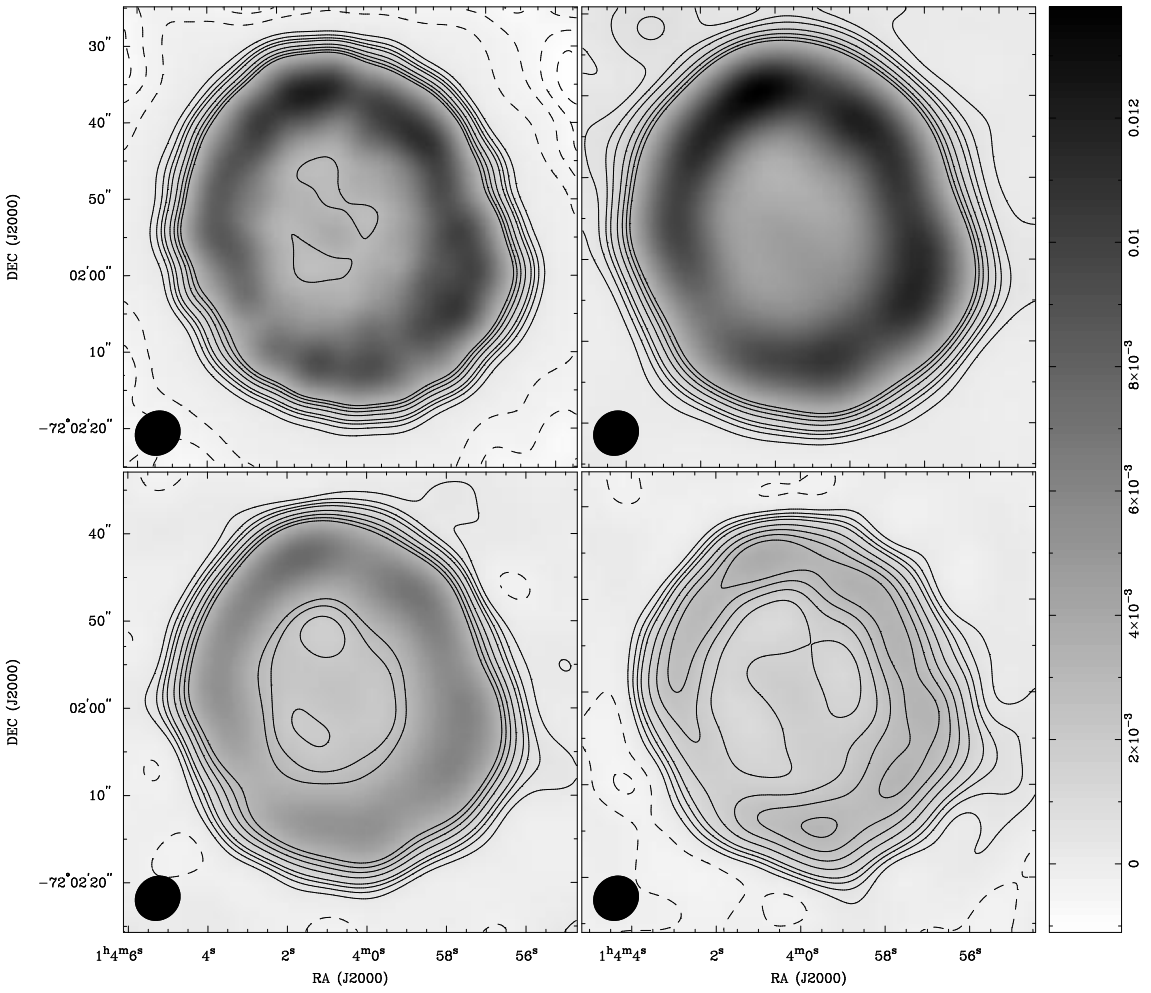

Figure 6.9: The multi-configuration ATCA images of SNR 1E 0102.2–7219 at the four observed frequencies (top left: 1472 MHz; top right: 2368 MHz; bottom left: 4790 MHz; bottom right: 8640 MHz). The three higher frequency images have been smoothed to the resolution of the 1472 MHz image (6.26 × 5.73 arcsec; p.a. −53.1 degrees) which is shown here for comparison. The (linear) grey-scale transfer function is indicated by the wedge on the right with intensity units of Jy/beam. The scale is the same in all four images. Contours have been overlaid at −10, −8, −6, −4, −3, −2, −1.5, −1, −0.75, −0.5, −0.25, 0.25, 0.5, 0.75, 1, 1.5, 2, 2.5, 3 mJy/beam.

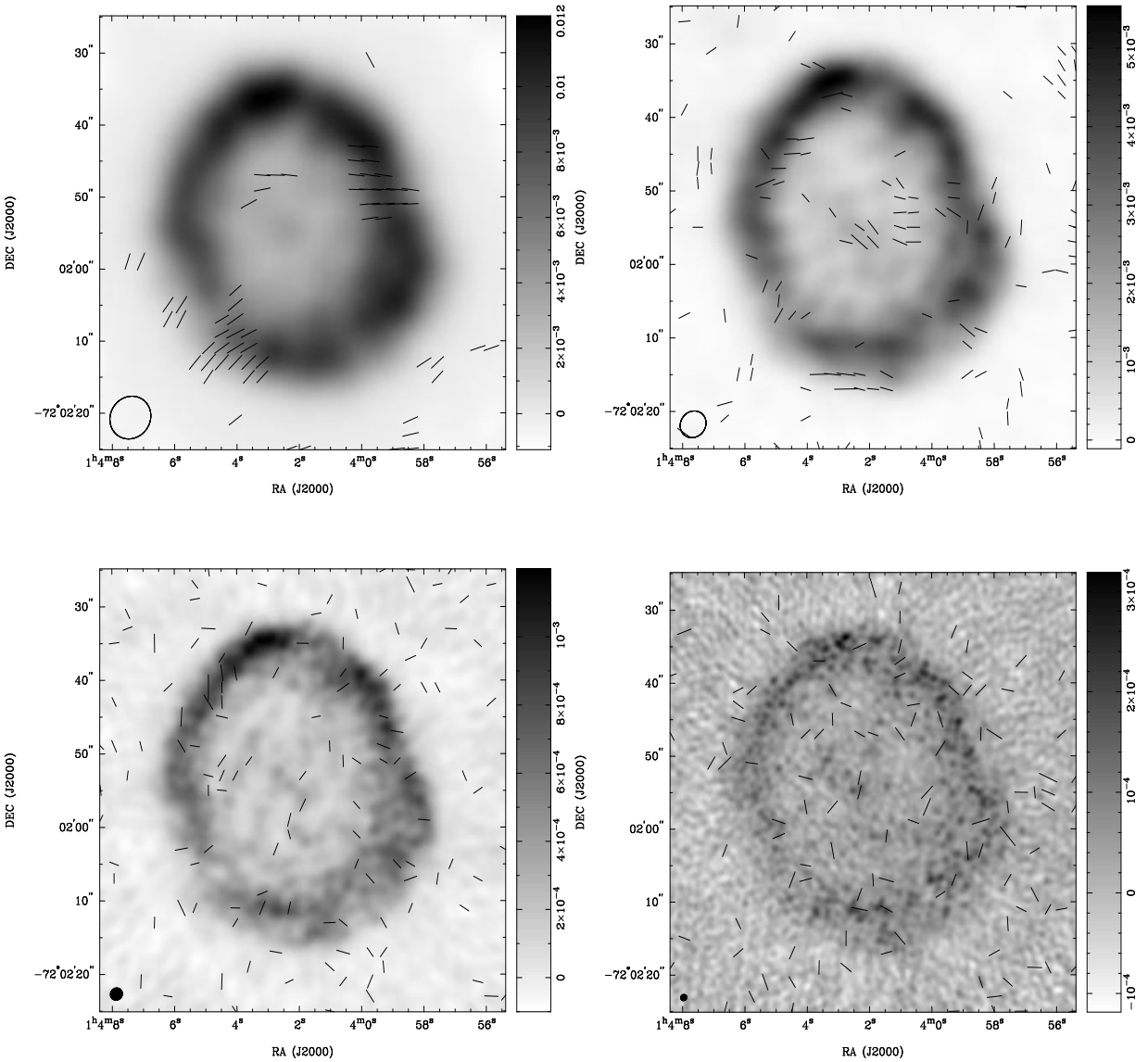

Figure 6.10: The multi-configuration total-intensity ATCA images of SNR 1E 0102.2–7219 at the four observed frequencies (top left: 1472 MHz; top right: 2368 MHz; bottom left: 4790 MHz; bottom right: 8640 MHz) with electric-field vectors overlaid. The (linear) grey-scale transfer function is indicated by the wedge on the right of each image with intensity units of Jy/beam. No significant polarized intensity was detected.

Table 6.3: Integrated flux densities of SNR 1E 0102.2–7219 in the SMC at the four observed frequencies.

Frequency (MHz)	Integrated Flux Density (Jy)
1472	0.25
2368	0.23
4790	0.14
8640	0.08

to be $\alpha = -(0.65 \pm 0.20)$. The errors quoted for α (in both cases) are formal errors from the best fit procedure. These figures are consistent with that expected for oxygen-rich SNRs ($\alpha \leq -0.3$).

Like all aperture synthesis interferometers, the ATCA does not sample on very short baselines. This can lead to an underestimate of the flux of a source in which much of the radio emission is spread over large angular scales. Although the shortest baseline measured in the ATCA data presented here was 61 m (approximately $3.5'$), this result accurately represents the flux present at all angular scales, since the measured flux at the higher frequencies (> 1 GHz) is consistent with the extrapolation of the lower frequency measurements.

6.6 Discussion

The radio data obtained with the MOST and ATCA alone raise a number of interesting astrophysical questions. In order to discuss some of these issues comparison with data taken at other wavelengths, including optical and X-ray, is essential.

6.6.1 The Radio Data

As mentioned earlier in this chapter, oxygen-rich SNRs are thought to result from the explosion of a massive star as a Type II supernova. The oxygen-rich material is thought to be CNO processed ejecta from deep within the stellar interior. Such SNRs are powered primarily by the energy associated with the shock produced by the supernova explosion. The shock interacts with the circumstellar material ejected from the progenitor star in the final stages before the explosion rather than interacting with the interstellar medium itself.

From a number of cuts through the preliminary 4790 MHz ATCA image of SNR 1E 0102.2–7219 at various position angles, such as those shown in Figure 6.4, we estimate the angular diameter of the outer shell of the radio emission to be approximately $(40 \pm 5)''$. Similar results were obtained from the more recent ATCA data at four frequencies.

These results agree well with observations at other wavelengths. Dopita et al.

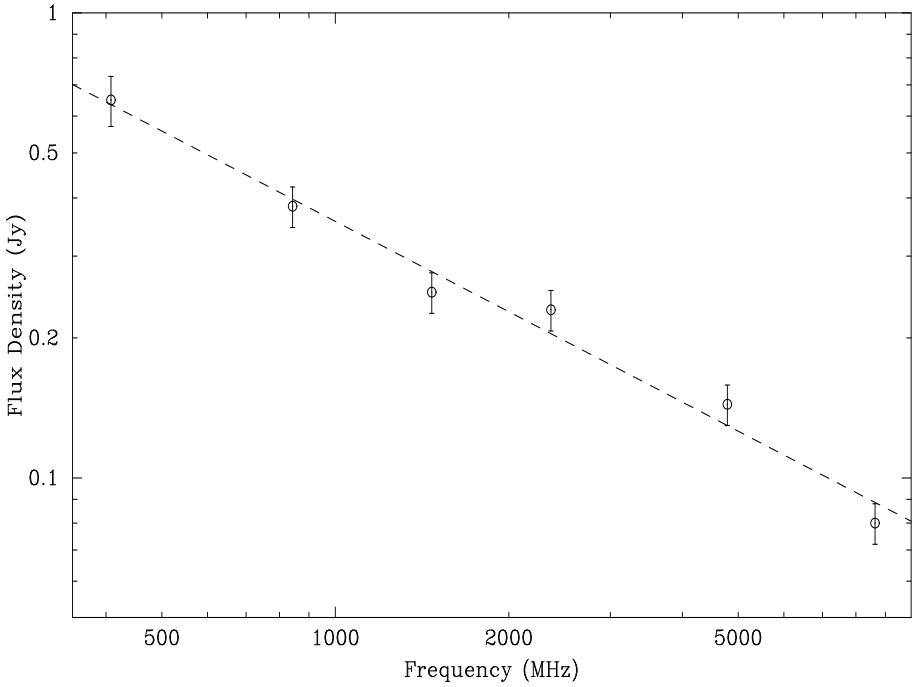

Figure 6.11: The radio spectrum of SNR 1E 0102.2-7219. The flux at frequencies > 1 GHz are from the multi-frequency ATCA data presented here, and an uncertainty of 10% (at each frequency) is assumed. The flux and associated uncertainties at 408 MHz and 843 MHz are from previously published observations (see text). The dashed line is the best-fit power-law spectrum to these data and a spectral index of $\alpha = -(0.65 \pm 0.20)$ was determined.

(1981), hereafter referred to as DTM, measured the diameter of the optical [O III] shell to be about 24″. DTM also point out that surrounding the bright [O III] filaments, which comprise the optical shell, is a region of very low surface brightness in both [O III] and Hα. They estimated the outer diameter of this so-called "emission hole" to be $35'' - 40''$. They attribute the region of reduced optical emission to suppression due to ionization of the circumstellar material by the passage of the supernova shock wave. Thus the region immediately behind the shock is assumed to be highly ionized, and the [O III] emission comes from the material only after it has begun to recombine well after the passage of the shock. This implies that the shock diameter is $\gtrsim 40''$. On the basis of these arguments DTM predicted the presence of an X-ray shell outside the optical emission hole. This was later confirmed by Tuohy & Dopita (1983) who reported that the *Einstein Observatory* HRI data (see Figure 6.13) do indeed show a strong X-ray shell with a diameter of about 40″. The X-ray data is discussed in further detail later in this chapter. The radio shell reported here is of essentially the same angular diameter as the shell of X-ray emission. The agreement between the radio observations presented here and DTM's model for the general morphology of the supernova shock is consistent with the interpretation of the radio emission from this SNR as synchrotron emission from ultrarelativistic electrons accelerated by the expanding supernova shock wave (e.g. Marscher & Brown 1978; Fedorenko 1983; Chevalier 1984). These data support the earlier claim that the angular diameter of the shock wave associated with SNR 1E 0102.2–7219 is indeed $\gtrsim 40''$.

The age of SNR 1E 0102.2–7219 remains uncertain. Taking the distance to the SMC to be 59 kpc (McNamara & Feltz 1980) gives a shock diameter $D \gtrsim 11.4$ pc. The diameter to age relationship of Clarke & Caswell (1976), $D = 0.9\,t^{2/5}$ with D in parsecs and t in years, then implies an age $t \gtrsim 570$ years (with large uncertainties). The empirical relationship, $t = 33\,D^{1.2}$ derived by Mills et al. (1984), gives a similar age estimate of $t \gtrsim 610$ years. These estimates are consistent with the age of ~ 1000 years identified by Tuohy & Dopita (1983) on the basis of the expansion velocity and angular extent of the optically emitting ring of material. Blair et al. (1989) used the data of Tuohy & Dopita (1983) and assumed constant expansion resulting in an age estimate of ~ 2000 years. However, this may be an overestimate because the shock could have already slowed significantly. In any event, the SNR is evidently young. The average shock speeds implied by the three age estimates are respectively, $\sim 10000\,\mathrm{km\,s^{-1}}$, $\sim 5500\,\mathrm{km\,s^{-1}}$ and $\sim 2300\,\mathrm{km\,s^{-1}}$.

The cuts through the preliminary ATCA 4790 MHz image provide an estimate of $(18 \pm 3)''$ for the angular diameter of the compact component of the radio emission. This component contributes some 15 mJy or ~14% of the total flux at 4790 MHz. There are at least two interpretations of this source: (1) a bright spot on the surface of the radio shell or (2) a central or core component inside the radio shell. If the compact component is a bright spot on the shell, it presumably corresponds to a region of enhanced acceleration, and is of no special interest. If however it is a core component, its identification could have important implications for the classification and interpretation of SNR 1E 0102.2–7219. Such core components, in supernova remnants which also exhibit shell structures, are often referred to as "plerions" and are believed to be

associated with a remnant pulsar produced in the supernova explosion. Of course not all plerions are core components – the Crab is a well-known plerion which does not appear to be surrounded by a shell. Plerionic radio emission is thought to be the result of electrons and positrons accelerated by the rotation of the pulsar, and radiating synchrotron emission in a diffuse but relatively compact nebula (e.g. Marscher & Brown 1978; Pacini & Salvati 1981; Shklovskii 1981; Bandiera, Pacini & Salvati 1984).

One of only two other oxygen-rich SNRs which exhibits a compact, centre-filled morphology is G292.0+1.8. A detailed study of this SNR was undertaken by Braun et al. (1986) who concluded that the apparent "Crab-like" appearance was *not* due to a pulsar-driven synchrotron nebula but rather to slow and clumpy ejecta encountering the reverse shock. The centre-filled morphology is interpreted as being due to efficient acceleration in just a small part of the expanding shock and G292.0+1.8 is not a member of the plerionic class. The compact component of SNR 1E 0102.2–7219 could also be interpreted as being due to acceleration at a reverse shock in the ejecta.

If the compact component is identified as being plerionic, SNR 1E 0102.2–7219 would be only the second oxygen-rich SNR to exhibit both a clear shell component and a plerionic core component, and thus belong in the class of plerionic composite SNRs (Weiler 1983; Weiler 1985a,b; Weiler & Sramek 1988). The first such SNR is 0540–693 (Manchester, Staveley-Smith & Kesteven 1993). Comparison of the 4790 MHz image and the [O III] image of SNR 1E 0102.2–7219 of DTM suggests that there is a region of enhanced [O III] emission corresponding to the compact radio component. This is consistent with the plerionic interpretation of the compact component. There is no obvious corresponding feature in the X-ray image from *Einstein* (Garcia et al. 1990) but this is not surprising given the limited resolution and sensitivity of the X-ray data. Hughes (1994) has undertaken a detailed study of the *ROSAT* X-ray data (discussed later in this chapter) which provides only weak support for the presence of a plerionic core component. The high resolution ATCA radio observations at the other frequencies clearly resolved the radio shell but provided little support for the presence of any compact components. As mentioned, there is some suggestion of enhanced radio emission in the region *inside* the radio shell at 8640 MHz but it should be remembered that this image is rather noisy and there is a significant uncertainty as to the nature of this emission. If the spectra of the compact and shell components could have been resolved and were similar then the obvious implication is that the compact component is just a bright spot on the shell. On the other hand, the spectra of plerionic SNRs are typically flatter ($\alpha \geq -0.3$) than the observed spectrum of SNR 1E 0102.2–7219 ($\alpha \approx -0.7$). The relatively steep spectrum derived here from observations of the total flux from SNR 1E 0102.2–7219 suggests that if the compact component is plerionic, it contributes relatively little to the total flux at frequencies ≤ 5 GHz. If the contribution of the compact component to the total flux could have been determined to increase with frequency then this would argue strongly for the plerionic interpretation.

Tuohy & Dopita (1983) found He II emission in the diffuse halo which surrounds this SNR. They concluded that the He II emission was either from an H II region created by the UV flash from the supernova explosion which produced SNR 1E 0102.2–7219, or that the excitation was caused by intense UV emission from the remnant itself. The

MOST image of SNR 1E 0102.2–7219, shown in Figure 6.1, shows that the SNR may be embedded in N76, an H II region centered to the south-west of the remnant. Garnett et al. (1991) also found He II (λ4686) emission from N76. This emission is centered on a particular star in N76 which is some distance from SNR 1E 0102.2–7219. It is not clear if there is any association between the He II emission observed by Garnett et al. (1991) and that observed by Tuohy & Dopita (1983). Garnett et al. (1991) discuss the possible role of shock excitation in the production of He II nebulae. Modelling indicates that the strength of the He II emission is strongly dependent on the shock speed with a maximum at around 120 km s^{-1} then dropping sharply before slowly increasing at very high shock speeds. Thus the He II emission observed by Garnett et al. (1991) could be attributed to the shock wave of an SNR (not 1E 0102.2–7219). However, they found no other indicators of shock excitation. Our observations show no evidence of 4790 MHz continuum radio emission at the position of the He II emission observed by Garnett et al. (1991) within the 3σ limit of 0.23 mJy/beam. Furthermore the electron temperature in N76 is roughly 15 000 K (Dufour & Harlow 1977) which is not significantly higher than that in other H II regions with similar oxygen abundance. The electron temperature could reasonably be expected to be much higher than this were a supernova shock wave present in the region.

6.6.2 Comparison with Data at Other Wavelengths

Optical

A combined [O III] and Hα image of SNR 1E 0101.2–7219 is shown in Figure 6.12 where the green indicates [O III] emission and the reddish colouring represents Hα emission. The image (kindly supplied by Dr M.A. Dopita, MSSSO) was taken with the 2.3 m telescope on Siding Spring Mountain.

The extent of the [O III] emission is about 24″ in diameter and corresponds to the central region if the ATCA radio images. Surrounding this central [O III] emission is a region of low emission which is the "so-called" emission hole of diameter about $35-40''$. As discussed the outer radio shell has a diameter of about 40″ which agrees well with this region of low-surface brightness.

X-Ray

At X-ray wavelengths, two major imaging studies have been undertaken using instruments on-board the *Einstein* satellite where the first identification of this object was made at X-ray wavelengths by Seward & Mitchell (1981). More recently, higher resolution images have been made using the *ROSAT* satellite and a detailed study has been undertaken by Hughes (1994) who modelled the X-ray data and compared the model to observations at radio and optical wavelengths.

Figure 6.13 shows the X-ray image obtained from the *The Einstein Observatory Database of HRI X-ray Images* (Garcia et al. 1990). This image shows a fairly complete shell of X-ray emission, with very little spatial variation of the shell and also with little

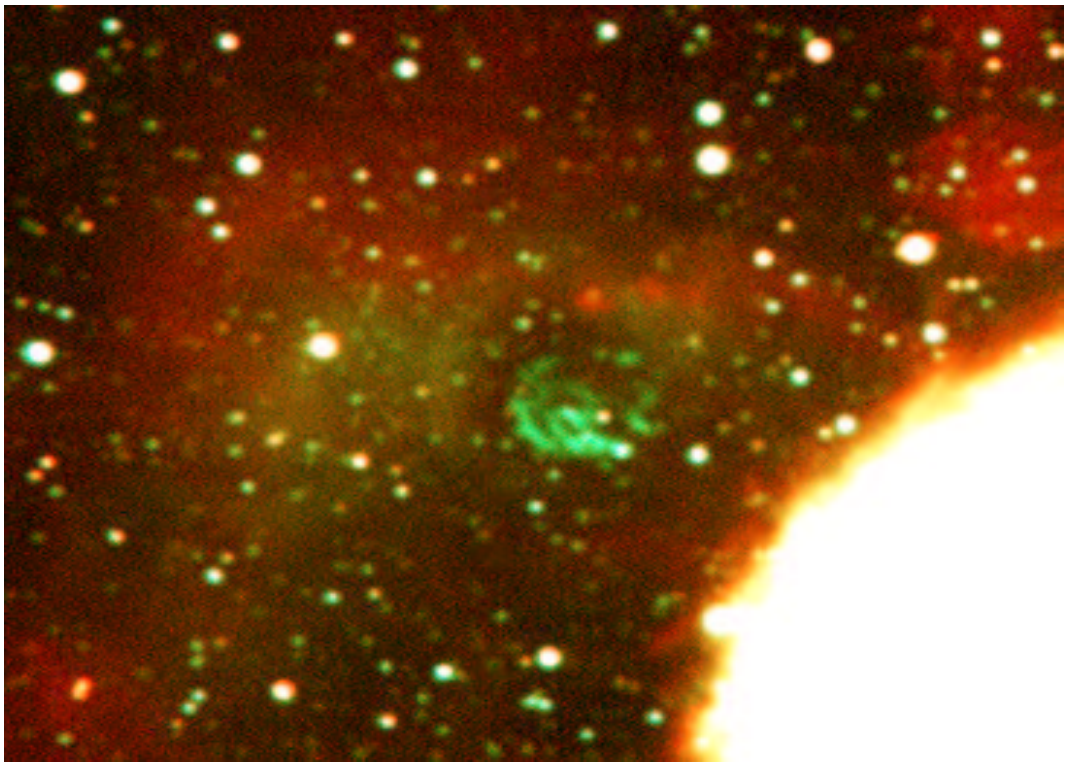

Figure 6.12: A combined [O III] and Hα image of SNR 1E 0101.2–7219, taken with the 2.3 m telescope on Siding Spring Mountain. The green indicates the [O III] emission and the reddish colouring represents Hα emission. The bright source in the south-west corner of the image is the large, extended H II region, N76, which is also seen in the MOST 843 MHz radio image shown in Figure 6.1.

azimuthal variation in intensity. There is no obvious compact central component which may reasonably be expected if the SNR had a pulsar-driven central component.

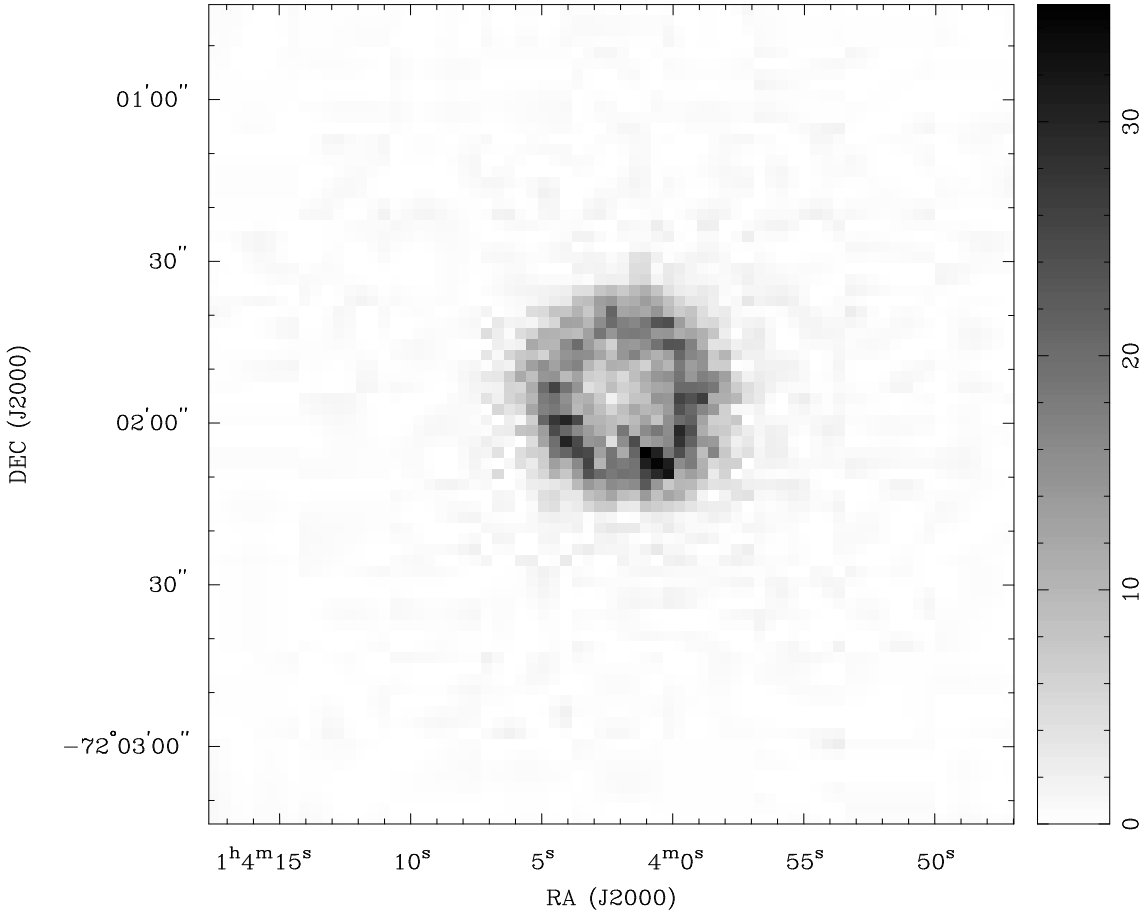

Figure 6.13: The *Einstein Observatory* HRI X-ray image of SNR 1E 0101.2–7219. The image units are counts/pixel with the major feature being the almost complete shell of X-ray emission. There is little emission corresponding to a compact central component. The image was regridded from B1950.0 coordinates to J2000.0 using the $\mathcal{AIPS}$ task `REGRD`.

A more recent image has been obtained with the *ROSAT* HRI and is shown in Figure 6.14. This image was obtained from the *ROSAT* data base. Again, the most noticeable feature is the almost complete shell of X-ray emission with little azimuthal variation. There is little evidence for a relatively strong plerionic component.

Hughes (1994), using the *ROSAT* HRI undertook dedicated observations of SNR 1E 0102.2–7219 during 1991. This (deconvolved) image showed a strongly limb-brightened but clumpy shell. There is only weak evidence for any compact central component at X-ray wavelengths. Detailed modelling of the X-ray emission was also undertaken by Hughes (1994) and he concluded that the single component models (either shell or ring shaped) provided a good fit to the observed data. A better fit to the observed data was found by using both a shell-like and a ring-like component initially

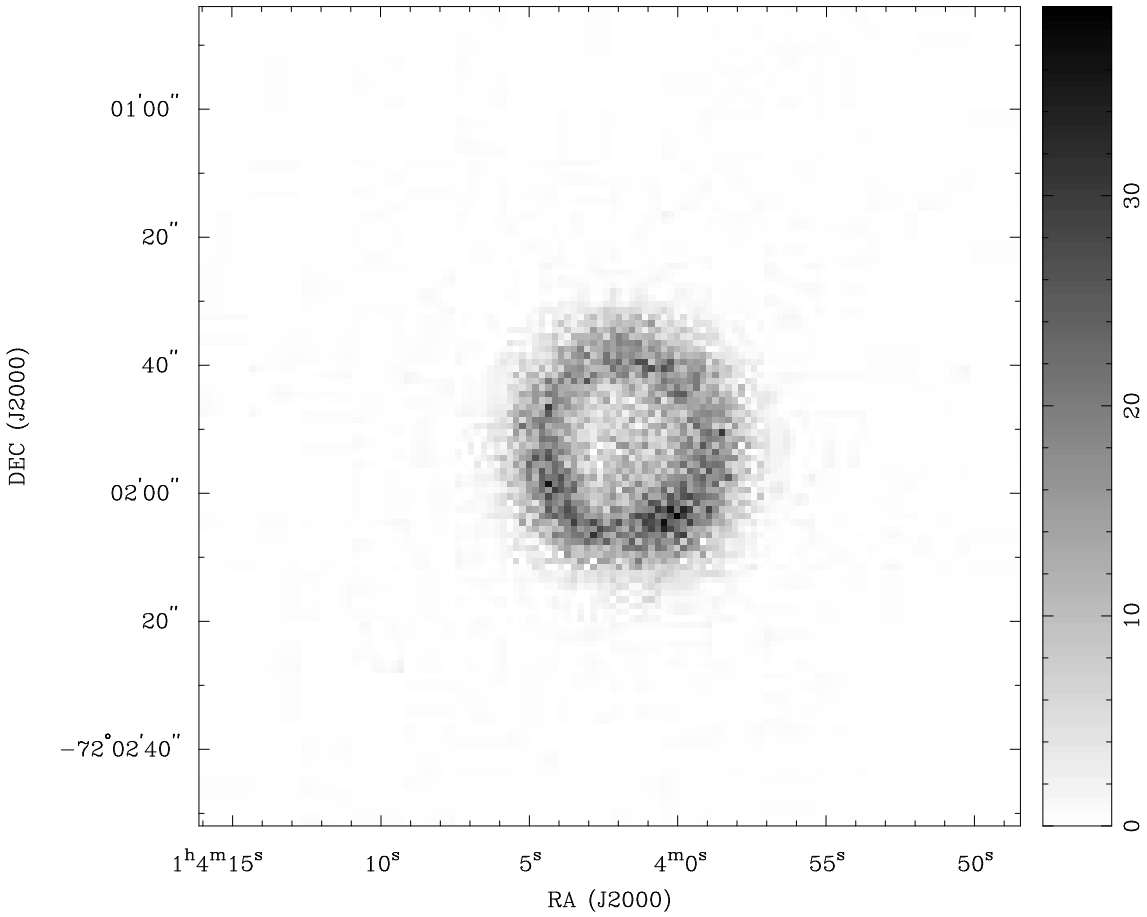

Figure 6.14: The *ROSAT* Observatory HRI X-ray image of SNR 1E 0101.2–7219. The image units are counts/pixel with the major feature being the almost complete shell of X-ray emission. There is little emission corresponding to a compact central component and is very similar to the *Einstein* image.

both components were concentric and with the same azimuthal density variation. It was found that with the addition of three additional parameters: radius, thickness and normalization of the shell component and significant improvement was made over the single component model. By comparison of the modelled data and the observation data, it was found that there were features on spatial scales of $\leq 5''$. These were modelled as six discrete clumps. From this model, Hughes (1994) states that roughly 39% of the HRI emissivity comes from the ring, 50% from the shell component and about 11% from the clumped component although he notes that due to limited statistics and the instrumental resolution this latter component should be viewed as being merely a lower limit.

Further, Hughes (1994) discusses the correlation between the above X-ray data and the preliminary 4790 MHz ATCA radio data presented here. He notes that the correlation does not seem particularly good. Some of the more important differences are that the brightest part of the radio image (at all four frequencies) is to the north-east whereas the X-ray shell shows a minimum in the quadrant. The other important morphological difference is that radio shell seems somewhat asymmetric which does not appear in the X-ray data. More interesting, is that there does appear to be a weak X-ray clumped component near the position of the relatively strong central component seen in the preliminary 4790 MHz ATCA image although this clump only contains about 1.7% of the total SNR X-ray flux. This is about an order of magnitude less than the flux of the X-ray plerionic core component which is present in the LMC remnant SNR 1E 0540–693 after corrections for the different distances are applied to the two SNRs. Based on the more recent radio data, it does now seem likely that the possible compact central component is more likely to be a bright spot on the SNR shell seen in projection.

6.7 Summary

The ATCA observations presented in this chapter provided the first high angular resolution, multi-frequency observations of SNR 1E 0102.2–7219. A spectral index of $\alpha = -(0.65 \pm 0.20)$ was determined, consistent with that expected for oxygen-rich SNRs.

The image obtained from the initial ATCA 4790 MHz observations suggested the presence of a compact plerionic component. However, the follow-up multi-frequency observations do not support this identification. Subsequent reports of observations at other wavelength bands (particularly X-ray) have also not found evidence for a plerionic component. The radio shell has morphological features common to all observed wavelengths, with an apparent "gap" in the shell clearly seen to the south-east. The relatively weak flux density of this SNR has precluded the measurement of polarized intensity.

The *Einstein* and *ROSAT* high-resolution X-ray images show an almost complete shell of X-ray emission, but lack sufficient angular resolution to distinguish significant morphological features or variation in X-ray intensity. A recent study by Gaetz et al.

(2000) used the *Chandra X-ray Observatory* to produce the first X-ray image of SNR 1E 0102.2–7219 with angular resolution comparable to that of the ATCA radio observations. In a comparison between the *Chandra* X-ray results, the preliminary ATCA 4790 MHz data presented here and optical images, Gaetz et al. (2000) conclude that for the first time *Chandra* has imaged the outer blast wave and a stronger inner-ring of X-ray emission. The outer ring of X-ray emission has a larger radius than the radio shell, whereas the inner ring of X-ray emission is inside the radio shell and corresponds to an ionizing reverse shock. This interpretation is consistent with the optical study undertaken by Dopita et al. (1981) and with the results presented in this chapter which were drawn primarily from a comparison of radio and optical data.

Such observations, and the comparisons they afford, offer real advances in the the understanding of the dynamical processes which occur as an expanding supernova shock interacts with circumstellar material and ejecta. A comparison of the more recent multi-frequency ATCA observations with the *Chandra* X-ray data and with optical data is beyond the scope (and time constraints) of this thesis, but is a very high priority for the future. Further dedicated radio observations may be warranted, particularly at 5 and 8 GHz, to obtain higher dynamic range images at frequencies with comparable angular resolution to the X-ray data.